Vibrational properties of $CuInP_2S_6$ across the ferroelectric transition

Sabine N. Neal,[1] Sobhit Singh,[2] Xiaochen Fang,[2,3] Choongjae Won,[4] Fei-ting Huang,[2,3] Sang-Wook Cheong,[2,3,4] Karin M. Rabe,[2] David Vanderbilt,[2] and Janice L. Musfeldt[1,5,*]

[1]*Department of Chemistry, University of Tennessee, Knoxville, Tennessee 37996, USA*
[2]*Department of Physics and Astronomy, Rutgers University, Piscataway, New Jersey 08854, USA*
[3]*Rutgers Center for Emergent Materials, Rutgers University, Piscataway, New Jersey 08854, USA*
[4]*Laboratory for Pohang Emergent Materials and Max Plank POSTECH Center for Complex Phase Materials, Pohang University of Science and Technology, Pohang 790-784, Korea*
[5]*Department of Physics and Astronomy, University of Tennessee, Knoxville, Tennessee 37996, USA*

(Dated: August 5, 2021)

In order to explore the properties of a two-sublattice ferroelectric, we measured the infrared and Raman scattering response of $CuInP_2S_6$ across the ferroelectric and structural phase transitions and compared our findings to a symmetry analysis and calculations of phase stability and lattice dynamics. In addition to uncovering a large hysteresis region surrounding the ferroelectric transition temperature T_C, we identify the vibrational modes that stabilize the polar phase and confirm the presence of two domains corresponding to "up" and "down" polarizations. Below T_C, a poorly understood structural phase transition at T_S is characterized by more subtle peak splitting and shifting in the low frequency out-of-plane Cu- and In-containing modes, another large hysteresis region, and significant underlying scattering. Combined with imaging of the room temperature phase separation, this effort lays the groundwork for studying $CuInP_2S_6$ under external stimuli and in the ultra-thin limit.

INTRODUCTION

The past decade has witnessed exceptional progress in revealing the potential and inner workings of complex chalcogenides, especially those belonging to the metal phosphorous trisulfide family (MPS_3, with M = Mn, Fe, Ni) [1–3]. Exciting properties under external stimuli include sliding, metallicity, piezochromism, and superconductivity under pressure [4–7], reentrant phases in high magnetic fields [8–11], tunable band gaps [12], and strongly anisotropic thermal conductivity [13]. These systems can also be exfoliated into few- and single-layer sheets that host novel magnetic excitations and states as well as symmetry breaking [14–23]. While simple metal site substitution is well-studied in the MPS_3 series, bimetallic substitution is relatively unexplored even though lower symmetry may promote useful properties such as ferroelectricity [24–26] along with different types of structural phase transitions. Dual-sublattice analogs such as bimetallic $CuInP_2S_6$ and $AgInP_2S_6$ offer flexible platforms for the discovery of tunable states of matter under external stimuli and the development of structure-property relations. For instance, $CuInP_2S_6$ hosts a quadruple-well potential with two distinct polar phases and four different polarization states under strain [27, 28].

$CuInP_2S_6$ is a layered van der Waals system with a paraelectric $\leftrightarrow$ ferroelectric transition near T_C = 310 K [29–35]. Although the terms "ferrielectric" and "ferroelectric" are both used in the literature [27, 29, 30, 33, 34, 36–39], $CuInP_2S_6$ is formally a ferroelectric since there is only one unstable polar mode - in this case belonging to the Cu sublattice. (By contrast, a ferrielectric would have two unstable polar modes.) In other words, the opposite polar displacement of the In sublattice is a consequence of the polar displacement of Cu^+ ions. In any case, the polarization in $CuInP_2S_6$ is stable and switchable, although polarization switching under high bias is associated with Cu^+ ion mobility [34, 40]. The latter has a two-step path that involves both in-plane and out-of-plane hopping of the Cu^+ ions [40]. In the high temperature paraelectric phase, the system is in the $C2/c$ space group, whereas the polar phase has Cc symmetry [36]. Individual layers of $CuInP_2S_6$ consist of Cu^+ and In^{3+} ions surrounded by sulfur octahedra with P–P dimers filling the octahedral voids. In addition to providing an explanation for the high bias ionic conductivity, the symmetry reduction from $C2/c \rightarrow Cc$ is thought to occur with ordering of the copper occupancies in addition to the primary driver - which is distortion of cations from their centrosymmetric positions [36]. Variable temperature Raman scattering confirms order-disorder character across the ferroelectric transition [41], although overall, this transition is poorly understood.

Because T_C is just above room temperature, there are a number of intriguing properties at 300 K. For example, $CuInP_2S_6$ displays a room temperature electrocaloric effect that may prove useful for solid-state refrigeration [42]. The system also hosts sizable intrinsic negative longitudinal piezoelectricity [27, 43]. Further, $CuInP_2S_6$ single crystals exhibit polar domain structure that gets smaller and then disappears in flakes thinner than 50 nm [34, 44, 45]. $CuInP_2S_6$ is also being prepared in thin film form. In fact, when sandwiched with germanene as a two-dimensional van der Waals heterostructure, electric field can drive a metal-semiconductor transition via control

* musfeldt@utk.edu

over the polarization direction [46]. $CuInP_2S_6$ has been incorporated (along with MoS_2) in a negative capacitance field effect transistor as well [47]. Dielectric studies of crystals reveal a broad relaxation near 150 K, although the exact position, amplitude, and shape depends upon the measurement frequency [36]. This relaxation is attributed to a dipolar glass transition [36]. Finally, we note that this system hosts a first-order monoclinic $\leftrightarrow$ triclinic structural transition at 4 GPa [29].

In this work, we combine infrared absorption and Raman scattering spectroscopies to reveal symmetry-breaking and local lattice distortions across the ferroelectric and structural phase transitions in $CuInP_2S_6$. We compare our findings with complementary lattice dynamics calculations, mode displacement patterns, and an analysis of the energy landscape. Interestingly, we identify several different infrared- and Raman-active modes in this bimetallic system that appear below the ferroelectric transition, although of course only the odd-symmetry features contribute to the development of polarization. Comparison with the MPS_3 family of materials reveals that bimetallic A-site substitution supports a polar ground state. On the other hand, the structural phase transition is characterized by subtle peak splitting and shifting of low frequency out-of-plane Cu- and In-containing modes. We attribute the pronounced broadening and hysteresis across each of these transitions to bimetallic substitution on the metal site as well as the Cu site disorder. We further investigate the tendency toward chemical-phase separation using a combination of vibration spectroscopies as well as piezoforce and transmission electron microscopies uncovering the signatures of the highest quality $CuInP_2S_6$ crystals and imaging their two polarization domains.

METHODS

Single crystals of $Cu_{1-x}In_{1+x/3}P_2S_6$ were grown by vapor transport methods as follows. Copper powders, indium shots, a phosphorus lump, and sulfur flakes were loaded into an evacuated quartz tube with $\approx 10^{-5}$ torr pressure and then heated with temperature gradient between both ends of the quartz ampule. The sealed tube was held at $\approx$1023 K for 10 days and then cooled to room temperature. The single crystal flakes were mechanically extracted from the entangled bulk. To confirm sample quality and purity, we performed energy dispersive x-ray analysis (EDX), piezoforce microscopy, and transmission electron microscopy. The vertical piezoforce microscopy (PFM) experiments were performed on freshly exfoliated surfaces of $CuInP_2S_6$ using the MultiMode^{TM} atomic force microscope by Veeco/Digital Instruments. Thermally cured gold paste was used to mount the sample and act as the bottom electrode. All PFM measurements were conducted using between 3 and 5 V a.c. The voltage was applied to a conducting contact mode AFM tip, and the bottom electrode was grounded. The vertical piezoelectric response signal was extracted using a NanoScope^{TM} controller and a lock-in amplifier. Crystal structure, electron diffraction and domains were examined by JEOL-2010F field-emission transmission electron microscopy (TEM) in plane-view specimens. $In_{4/3}P_2S_6$-containing regions were observed by selecting (002) spots of $In_{4/3}P_2S_6$.

Prior to our spectroscopic measurements, the sample was exfoliated to reveal a clean, smooth surface that was adhered to a round pinhole aperture. Infrared measurements were performed using a Bruker IFS 113V infrared spectrometer equipped with a low noise He-cooled bolometer detector over the frequency range of 20-700 cm^{-1} with 2 cm^{-1} resolution. The measured transmittance was converted to absorption: $\alpha(\omega) = -\frac{1}{d}\ln(\mathcal{T}(\omega))$, where $\mathcal{T}(\omega)$ is measured transmittance, and d is the crystal thickness. Raman scattering measurements were carried out on a LabRAM HR Evolution Raman spectrometer over a 50-750 cm^{-1} frequency range using an exictation wavelength of 532 nm at a power of 0.1 mW, an 1800 line/mm grating, and a liquid N_2 cooled CCD detector. In each case, an open flow cryostat provided temperature control.

All the first-principles density-functional theory (DFT) calculations were performed using the Projector Augmented Wave (PAW) method as implemented in the Vienna Ab initio Simulation Package (VASP) [48–50]. The number of valence electrons in the considered PAW pseudopotentials were 11 ($3d^{10}\,4s^1$), 3 ($5s^2\,5p^1$), 5 ($3s^2\,3p^3$), and 6 ($3s^2\,3p^4$) for Cu, In, P, and S atoms, respectively. The exchange-correlation functional was computed using the generalized-gradient approximation (GGA) as parameterized by Perdew-Burke-Ernzerhof (PBE) [51]. The zero-damping D3 method of Grimme (PBE-D3) was employed to describe the weak van der Waals interactions between the $CuInP_2S_6$ layers [52]. This method has been reported to correctly predict a wide range of physical and chemical properties of $CuInP_2S_6$ [53, 54]. The energy convergence criterion for self-consistent DFT calculations was set at 10^{-7} eV and force convergence criterion for relaxation of atomic coordinates was set at 10^{-3} eV/Å. The reciprocal space was sampled using a Monkhorst-pack k-mesh [55] of size 8×8×4 along with a kinetic energy cutoff of 650 eV for the plane waves.

The optimized lattice parameters and cell angles of the paraelectric $C2/c$ phase are $a = b = 6.069$ Å, $c = 13.159$ Å, $\alpha = \beta = 94.5^0$, and $\gamma = 119.9^0$. The ferroelectric Cc phase was obtained after applying a polar Γ_2^- distortion on the high-symmetry $C2/c$ phase. A further free relaxation was performed of the local minimum structure (Cc) shown in Fig. 1. The resulting cell parameters and cell angles of the Cc phase are $a = b = 6.112$ Å, $c = 13.360$ Å, $\alpha = \beta = 94.3^0$, and $\gamma = 120.0^0$. The PHONOPY package was employed to calculate the phonon frequencies and phonon eigenvectors of the optimized structures at zone center using the finite-displacement approach [56]. The Bilbao Crystallographic Server was utilized to analyze the symmetry of phonon modes [57].

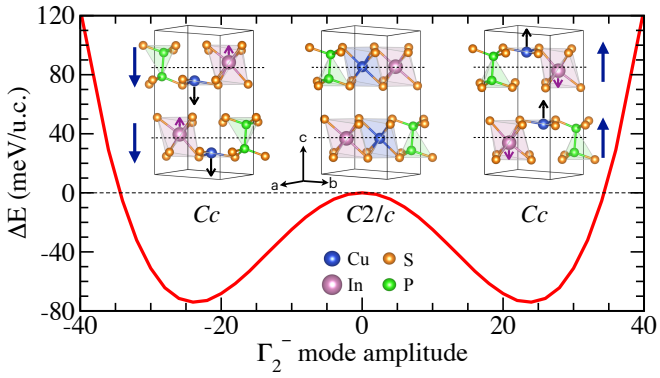

FIG. 1. The double-well potential energy profile computed by freezing the polar Γ_2^- phonon mode in the paraelectric phase as a function of the phonon distortion amplitude. Crystal structures of the paraelectric ($C2/c$) and ferroelectric (Cc) phases of $CuInP_2S_6$ are shown in the inset. Black arrows denote the displacement of Cu ions corresponding to the Γ_2^- mode distortion. Purple arrows denote the relatively small displacement of In ions. The net polarization of individual $CuInP_2S_6$ layers is along the direction of the blue arrows.

The theoretical infrared (IR) spectra were calculated by computing the mode dynamical charge associated with each phonon eigendisplacement, and the theoretical Raman spectra were simulated by appropriately averaging the Raman activity tensor calculated for each Raman-active phonon eigenmode at zone center [58].

RESULTS AND DISCUSSION

A. Analyzing the symmetries and properties of $CuInP_2S_6$

1. *Energy landscape and ferroelectricity*

Before we present our temperature-dependent investigations of the infrared and Raman measurements and discuss the chemical phase separation in $CuInP_2S_6$, let us start by briefly describing the essential details of the crystal structure, ferroelectricity, and vibrational properties of the paraelectric and ferroelectric phases of $CuInP_2S_6$. The inset of Fig. 1 shows the crystal structure of the paraelectric and two equivalent ferroelectric phases of $CuInP_2S_6$, which belong to space groups $C2/c$ (no. 15) and Cc (no. 9), respectively. The bulk unit cell of both phases contains two weakly interacting single layers of $CuInP_2S_6$, *i.e.*, 2 f.u., stacked along the c-axis. In the paraelectric phase, the vertically stacked $CuInP_2S_6$ layers are related by an in-plane C_2 rotation followed by a translation $\tau(c/2)$ operation along the c-axis. This structure resembles a lamellar structure composed of a sulfur framework in which the metal cations and P-P dimers fill the octahedral voids within each layer [30–32, 37, 59, 60]. The P-P dimers act as vertical pillars separating the top and bottom sulfur planes in each layer. By contrast, the Cu and In metal cations reside exactly at the midplane of the layers, marked by dashed horizontal black lines in the inset of Fig. 1, lying between two vertically stacked sulfur planes and passing through the P-P dimer at its half bond length within each $CuInP_2S_6$ layer.

The paraelectric phase is stable only at high temperatures ($T > 310\,K$) [29–32, 34, 36–38]. Below 310 K temperature, this phase transforms into a ferroelectric Cc phase having a net polarization primarily along the out-of-plane direction of each $CuInP_2S_6$ layer [30–32, 37, 60], which occurs due to the polar displacements of the Cu and In sublattices in an antiparallel fashion relative to the midplane of each $CuInP_2S_6$ monolayer, as shown in Fig. 1.

From the group theory perspective, the paraelectric and ferroelectric phases are related by a zone center polar optic phonon mode distortion, Γ_2^- mode (B_u symmetry). This mode is unstable in the paraelectric phase having frequency $50.3i\,\mathrm{cm}^{-1}$ and it primarily represents an in-phase vertical displacement of two Cu ions located in the adjacent $CuInP_2S_6$ layers, as denoted using two parallel black arrows in the insets of Fig. 1 (left and right panels). The calculated potential energy profile obtained by freezing the the Γ_2^- mode as a function of the phonon distortion amplitude is shown in Fig. 1. The magnitude of the energy barrier is comparable with the data reported in Refs. [27, 28]. Notably, in Refs. [27, 28], authors reported the presence of two polar phases (Cc) with four different (two high and two low) polarization states under local strain conditions. No local strain was applied in our work.

We find that, in response to the polar displacement of Cu ions ($\sim$1.54 Å), In ions exhibit a relatively small ($\sim$0.20 Å) but nonzero polar displacement in the antiparallel direction to that of the displacement of Cu ions, as shown by purple arrows in the insets of Fig. 1 (left and right panels). Such a behaviour of In sublattice has been attributed to the second-order Jahn-Teller effects [32, 37, 41]. Although, technically speaking, $CuInP_2S_6$ has two polar sublattices, Cu and In, yielding a ferrielectric ordering in each $CuInP_2S_6$ layer, only Cu sublattice has a polar instability. In displacement occurs as a response to the polar displacement of Cu ions. Therefore, it is more appropriate to refer $CuInP_2S_6$ as a ferroelectric material than a ferrielectric material.

We further compute the magnitude of the net polarization ($\mathbf{P}$) in the Cc phase using the Berry-phase approach [61, 62]. The theoretically obtained value is $\mathbf{P} = (0.13, 0.00, 3.43)\,\mu\mathrm{C/cm}^2$, which is in excellent agreement with the experimental data reported by Maisonneuve *et al.* ($P_z \sim 3.5\,\mu\mathrm{C/cm}^2$ at 150 K) [37]. Interestingly, our calculations predict a nonzero in-plane polarization component P_x, which has not been discussed in the existing literature, to the best of our knowledge.

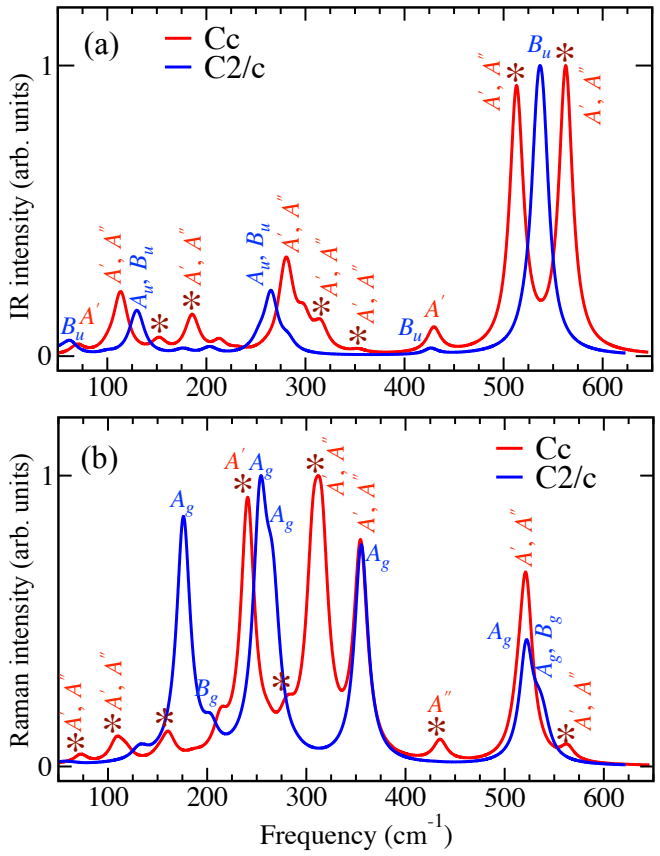

FIG. 2. The PBE-D3 calculated (a) IR and (b) Raman spectra for the paraelectric ($C2/c$) and ferroelectric (Cc) phases of $CuInP_2S_6$ at 0 K. The symmetries of the major infrared and Raman peaks in the paraelectric and ferroelectric phases are marked in blue and red, respectively. Some peaks are unmarked for clarity. These unmarked peaks contain mixed contribution from both IR active or both Raman active modes in their respective plots, similar to the marked peaks with mixed contributions. The $*$ sign denotes the potential signature modes of the ferroelectric phase, which are absent in the paraelectric phase. The intensities were normalized between zero and one (see Supporting Information [63] for more details).

2. *Selection rules in the paraelectric and ferroelectric phases*

Since the primitive cell contains two formula units, *i.e.*, 20 atoms/cell, there are sixty allowed phonon modes in $CuInP_2S_6$. According to the group theory, the allowed acoustic and optical vibrations at zone center can be described using the irreducible representations given below.

For the paraelectric phase ($C2/c$):

$$\begin{aligned} \Gamma_{\text{acoustic}} &= A_{\text{u}} \oplus 2B_{\text{u}}, \text{ and} \\ \Gamma_{\text{optical}} &= 14A_{\text{g}} \oplus 13A_{\text{u}} \oplus 16B_{\text{g}} \oplus 14B_{\text{u}}. \end{aligned} \tag{1}$$

For the ferroelectric phase (Cc):

$$\begin{aligned} \Gamma_{\text{acoustic}} &= 2A' \oplus A'', \text{ and} \\ \Gamma_{\text{optical}} &= 28A' \oplus 29A''. \end{aligned} \tag{2}$$

In the paraelectric phase, only A_{g} and B_{g} modes are Raman active while A_{u} and B_{u} optical modes are IR active. Instead, in the ferroelectric phase, all the A' and A'' optical modes are both Raman and IR active. Figure 2 shows the simulated IR and Raman spectra for the paraelectric (red) and ferroelectric (blue) phases. A list of the mode symmetries along with their frequencies is provided in the Supporting Information [63]. Some distinct features can be noticed in the simulated peak positions of the IR and Raman spectra which may facilitate the experimental identification of the paraelectric and ferroelectric phases. In Fig. 2, we marked some Raman and IR peak positions using $*$ signs, which denote the potential signature modes of the ferroelectric phase. For instance, the B_u IR peak located near frequency 536 cm^{-1} converts into two A' and A'' peaks located at frequencies $\sim$ 514 cm^{-1} and $\sim$ 564 cm^{-1} upon the paraelectric $\rightarrow$ ferroelectric phase transition [see Fig. 2(a)]. Also, a convoluted shoulder consisting of the A' and A'' modes develops near 316 cm^{-1} frequency in the ferroelectric phase, which is absent in the IR spectrum of the paraelectric phase.

On the other hand, the simulated Raman spectrum shows distinct signatures for the paraelectric and ferroelectric phases [see Fig. 2(b)]. For instance, new Raman peaks are predicted to appear in the ferroelectric phase near frequencies 72, 110, 311, 434, and 564 cm^{-1} which are absent in the Raman spectrum of the paraelectric phase. We note that in the ferroelectric phase, except for a few IR and Raman active peaks, most of the simulated peaks contain contribution from A' and A'' modes. This is mainly due to the fact that the difference in the frequency of most of the A' and A'' modes is practically negligible owing to the weak coupling between the adjacent $CuInP_2S_6$ layers. The simulated Raman spectra of the paraelectric and ferroelectric phases appears to be in decent agreement with our experimental data as well as with the data reported by Vysochanskii *et al.* [41]. A detailed comparison of the experimental and theoretical data is provided in the Supporting Information [63].

B. Vibrational properties of $CuInP_2S_6$ across the ferroelectric transition

1. *Infrared spectroscopy probes inversion symmetry breaking*

Figure 3 summarizes the infrared response of $CuInP_2S_6$ as a function of temperature. In order to analyze the development of polar phonons across T_{C}, we focus on the two frequency windows displayed in panels (a, d). High temperature phase spectra (300 K and above) are indicated in red and low temperature phase spectra (50 K and below) are indicated in blue.

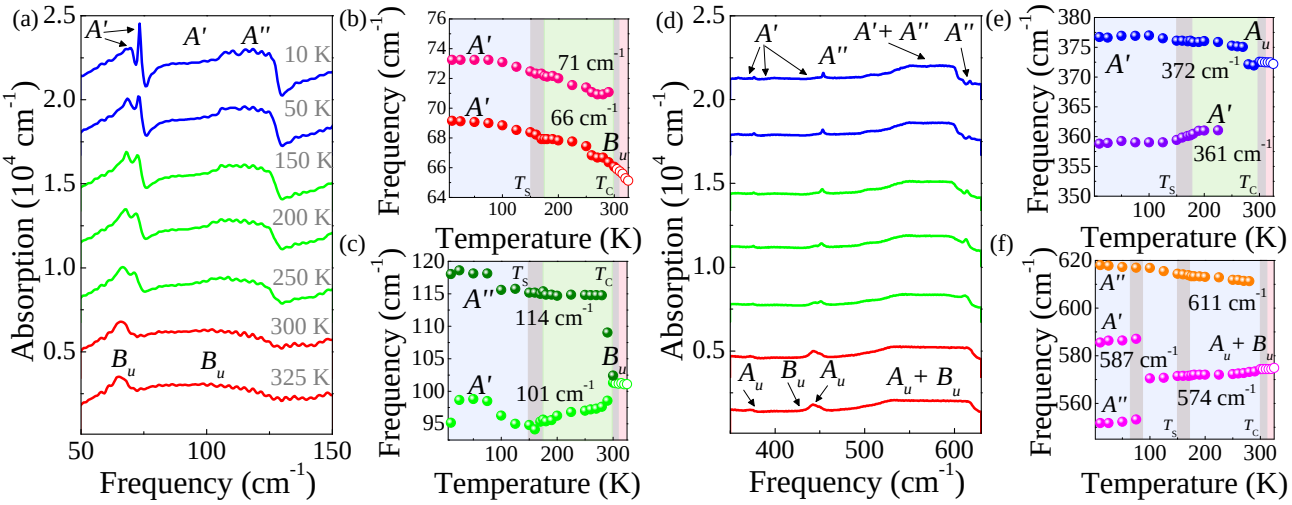

FIG. 3. (a, d) Close-up view of the far infrared response of single crystalline $CuInP_2S_6$ as a function of temperature (10-325 K). Note spectra collected at low temperature are depicted in blue, whereas spectra collected above 300 K are denoted in red. Panels (b, c) highlight the behavior of the ferroelectric phonons present in panel (a), whereas (e, f) display peak position vs. temperature of the ferroelectric modes highlighted in panel (d). The vertical gray bars define the structural transition regions and the open to closed data points represent a transition from the $C2/c \rightarrow Cc$ space group. There is a significant hysteresis effect depending upon direction of temperature sweep. These measurements are from 10 K up to 325 K.

TABLE I. Infrared-active vibrational modes that are sensitive to the ferroelectric phase transition in $CuInP_2S_6$. All values are in cm^{-1}. Corresponding DFT calculated frequencies (ω) are given in parentheses.

$C2/c$		Cc		
ω experiment	**symmetry**	**ω experiment**	**symmetry**	**displacement patterns**
65 (63)	B_u	-	-	in-plane twist of P-P dimers + out-of-plane vibration of S
-	-	66 (64)	A'	out-of-plane polar displacement Cu
-	-	71 (71)	A'	in-plane Cu + In + P + out-of-plane S
101 (100)	B_u	102 (102)	A'	out-of-plane rigid shift of P-P dimers (in-phase in adjacent layers) + out-of-plane vibration of S
-	-	114 (114)	A''	in-plane Cu + In + out-of-plane S
-	-	361 (354)	A'	in-plane Cu + S and out-of-plane P-P stretching
372 (359)	A_u	373 (355)	A''	in-plane Cu + S and out-of-plane stretching of P-P dimers (opposite phase in adjacent layers)
574 (540, 541)	B_u, A_u	553, 587, 611 (558, 563, 563)	A'', A', A''	in-plane P-P + in-plane S vibration vibration

At 325 K, there are two distinct phonons in the low frequency infrared response. These include a sharp B_u mode near 65 cm^{-1} as well as a very broad B_u mode centered around 101 cm^{-1}. As temperature decreases across $T_C = 310$ K, there is a noticeable splitting of the lower frequency B_u mode and the development of a shoulder on the 101 cm^{-1} feature. Figure 3 (b, c) highlights the response of these low frequency B_u symmetry phonons across T_C. Here, we see that the 65 cm^{-1} mode blueshifts systematically in the high temperature phase and splits below 310 K. The latter is due to a change in the space group from $C2/c$ in the high temperature phase $\rightarrow Cc$ in the ferroelectric phase. After the 65 cm^{-1} B_u symmetry structure splits, the assignments become $A' \oplus A'$ in the ferroelectric phase. The doublet sharpens and continues to blueshift with decreasing temperature. At the same time, the once-broad B_u symmetry mode at 101 cm^{-1} develops a shoulder below T_C. The lower frequency component evolves as an A' mode, and the higher frequency component at 114 cm^{-1} transforms to A'' symmetry [Fig.

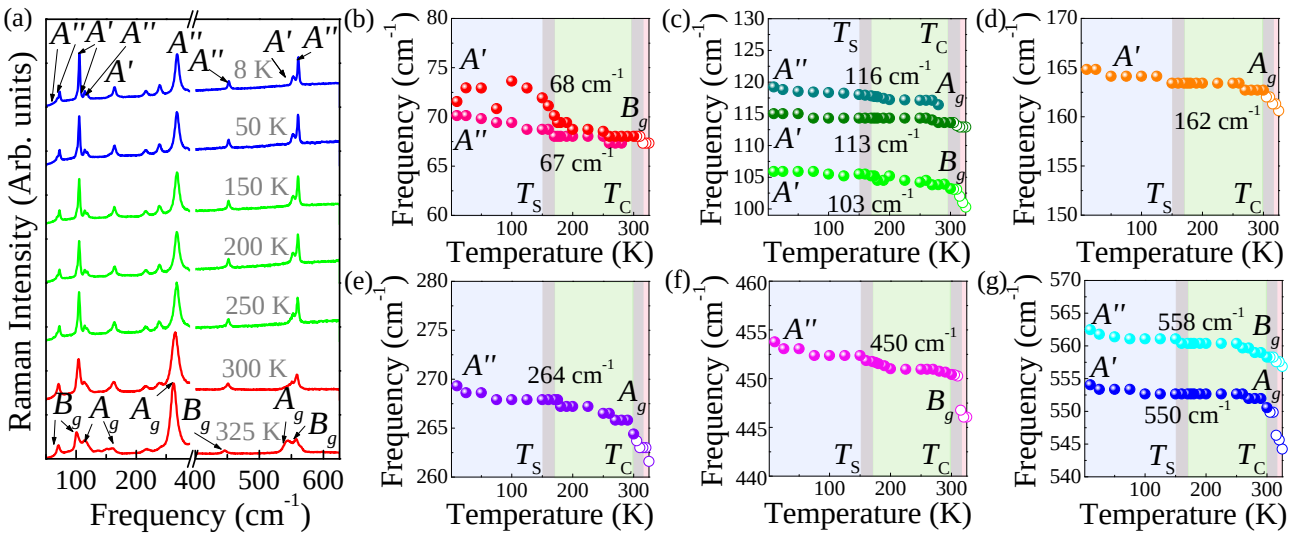

FIG. 4. (a) Raman scattering of single crystalline $CuInP_2S_6$ as a function of temperature between 8 and 325 K. Again, spectra collected above 300 K are denoted in red, those between 250 and 150 in green, and spectra collected below 50 K in blue. Panels (b-g) highlight the behavior of several different Raman-active modes, many of which are ferroelectric. The vertical gray bars define the structural transition regions. The open to closed data points also represent a space group transition from $C2/c \rightarrow Cc$. There is a significant hysteresis effect depending upon direction of temperature sweep. This is seen very clearly in the Raman scattering response when rendered as a contour plot [Supplemental Information]. The measurements shown here are from 10 K up to 325 K.

3(c)]. The A' branch redshifts below 310 K - a trend that continues to the 150 K structural phase transition - below which it blueshifts again. By contrast, the A'' branch has a sharp blueshift immediately below room temperature and continues to harden systematically to 10 K.

Figure 3(d) summarizes the infrared properties of $CuInP_2S_6$ in the 350 to 625 cm^{-1} range. Of the many vibrational modes present in the high temperature phase (red), only one is sensitive to T_C: the A_u symmetry mode at 372 cm^{-1} [Fig. 3(d, e)]. As T_C is crossed, a slight hardening occurs, followed by a change in space group from Cc to the ferroelectric $C2/c$ where an A_u feature becomes an A'' symmetry mode. Below T_C, this mode downshifts slightly before rising near 275 K, continuing to blueshift through base temperature. The presence of a small A' symmetry mode (361 cm^{-1}) can be seen in the low temperature phase near 225 K, with an overall redshift through base temperature. Figure 3(d, f) also shows a broad phonon centered 574 cm^{-1}, assigned as an $A_u \oplus B_u$ symmetry mode. This feature redshifts slightly through T_C where there is a symmetry change in the ferroelectric phase, with the new symmetry assigned as $A' \oplus A''$. Systematic redshifting persists through ≈100 K, where this broad feature splits slightly into two individual symmetry components, A' (587 cm^{-1}) and A'' (553 cm^{-1}). Both features redshift slightly to 10 K. The spectra shows a high frequency A'' mode that emerges at 611 cm^{-1} just below 300 K. The appearance of this feature is inline with our theoretical predictions. This mode sharpens and increases in frequency toward 10 K. A comprehensive table of mode assignments and displacement patterns is available in the Supporting Information.

The development of a polar state requires breaking of inversion symmetry, so we are naturally interested in the behavior of the odd-symmetry vibrational modes across T_C. Our infrared work demonstrates that $CuInP_2S_6$ hosts five polar modes in reasonable overall agreement with the results in Fig. 2(a). These include features near 65 and 103 cm^{-1} that split below T_C, the 372 cm^{-1} feature which blueshifts across the ferroelectric transition, and two additional features near 361 and 611 cm^{-1} (due to splitting) that appear in the low temperature phase. The predicted splitting of the high frequency mode above 500 cm^{-1} is consistent with the experimental data showing the 611 cm^{-1} phonon emerge from the broad feature centered at 575 cm^{-1} and the phonons below 300 cm^{-1} show dramatic shifts across the ferroelectric transition. All infrared-active polar modes, along with their symmetries and displacement patterns, are listed in Table I.

2. *Raman scattering spectroscopy across T_C*

Figure 4(a) summarizes the Raman scattering response of $CuInP_2S_6$ along with mode assignments for the various phonons in the high (red) and low (blue) temperature phases. Even-symmetry modes also change across T_C although they do not break inversion symmetry. For instance, the 68 cm^{-1} B_g symmetry mode splits just below room temperature to give two ferroelectric ($A' \oplus A''$ symmetry) modes [Fig. 4(b)]. The high frequency branch is relatively consistent in terms of size and position until

TABLE II. Raman-active vibrational modes that are sensitive to the ferroelectric phase transition in $CuInP_2S_6$. All values are in cm^{-1}. Corresponding DFT calculated frequencies (ω) are given in parentheses.

$C2/c$		Cc		
ω (**experiment**)	**symmetry**	ω (**experiment**)	**symmetry**	**displacement patterns**
67 (66)	B_g	-	-	in-plane Cu + P and out-of-plane S vibration
-	-	68 (64), 67 (70)	A', A''	out-of-plane Cu +S vibration
100 (108)	B_g	103 (102)	A'	out-of-plane In + P + S
113 (130)	A_g	114 (114), 116 (117)	A', A''	in-plane displacement Cu + In + S, out-of-plane S
161 (175)	A_g	-	-	in-plane Cu + P and out-of-plane S
-	-	162 (160)	A'	out-of-plane P-P + in-plane S
262 (254)	A_g	-	-	in-plane Cu + P + out-of-plane S
-	-	264 (263)	A''	in-plane S motion
446 (429)	B_g	450 (435)	A''	out-of-plane P + S
544 (534)	A_g	550 (558, 558)	A', A''	in-plane P-P stretching + S vibration
557 (539)	B_g	558 (562, 563)	A', A''	in-plane P-P + S vibration

150 K below which the peak position hardens toward 75 K and then softens again. The lower frequency branch systematically blue shifts toward base temperature. Figure 4(c) displays the behavior of the $A_g \oplus B_g$ high temperature doublet. The B_g component near 103 cm^{-1} hardens toward T_c then remains relatively constant (although the symmetry becomes A'). The A_g peak splits below 300 K, yielding an A' branch near 113 cm^{-1} and an A'' branch near 116 cm^{-1}. Moving on to the A_g feature at 162 cm^{-1} [Fig. 4(d)], we note a 4 cm^{-1} blueshift across the ferroelectric phase transition as the mode transitions to A' symmetry. The peak position remains relatively constant, shifting only slightly with decreasing temperature. Figure 4(e) displays the frequency vs. temperature trend for the A_g symmetry mode near 264 cm^{-1}. It blueshifts across the $C2/c \rightarrow Cc$ transition and is reclassified as A'' which has a fairly continuous up-shift to base temperature. The blueshift near the ferroelectric transition is much more dramatic in the B_g symmetry mode near 450 cm^{-1} [Fig. 4(f)]. Below 310 K, the feature hardens steadily until 150 K where there is a slight jump and then an overall blueshift toward base temperature. Finally, we turn our attention to Fig. 4(g) which displays the peak tracking for the high frequency $A_g \oplus B_g$ doublet. The lower frequency branch has a much more dramatic blueshift across T_C although both features track fairly systematically below 310 K, with a slight frequency upturn below 25 K. A full list of assignments as well as the relevant mode displacement patterns are available in the Supporting Information.

As previously mentioned, even-symmetry Raman-active modes change across T_C although they do not break inversion symmetry or contribute to the polarization in $CuInP_2S_6$. Our Raman scattering work reveals splitting of the 67 and 113 cm^{-1} phonons below T_C. This is inline with theory, showing the presence of new peaks in the ferroelectric phase. Other Raman active phonons including 100, 161, 262, 446, and the 544–557 cm^{-1} doublet evidence a transition from the paraelectric to ferroelectric phase due to sharp frequency shifts around 310 K. Frequency shifts are also evidenced in the predicted Raman spectra in Fig. 2(b). All Raman-active modes that are sensitive to T_C, along with their symmetries and displacement patterns are summarized in Table II.

3. *Bimetallic A-site substitution introduces ferroelectricity*

Returning to a comparison of MPS_3 systems (M = Mn, Ni, Fe) and dual sublattice analogs such as $CuInP_2S_6$ and $AgInP_2S_6$, we immediately see that the most important consequence of the bimetallic nature is the introduction of ferroelectricity. That T_C is slightly above room temperature is already providing the basis for a number applications. Examples include electrocaloric effects for refrigeration, negative longitudinal piezoelectricity, and a negative capacitance field effect transistor [42, 64]. Unfortunately, Cu site disorder demonstrably broadens the ferroelectric and structural phase transitions. This is seen very clearly in the Raman scattering response when rendered as a contour plot [Supplemental Information]. It also hinders the formation of larger polarization in $CuInP_2S_6$. The MPS_3 materials obviously do not have site disorder. They also lack ferroelectricity (although $MnPS_3$ may be ferrotorroidic) [65]. Another useful point of comparison in these structure-property relationships is $CrPS_4$, a related chalcogenide with slightly different stoichiometry and $C2$ symmetry [66]. This system appears to be both polar and chiral. In this system, there is no A-site disorder, but the P–P dimer is absent.

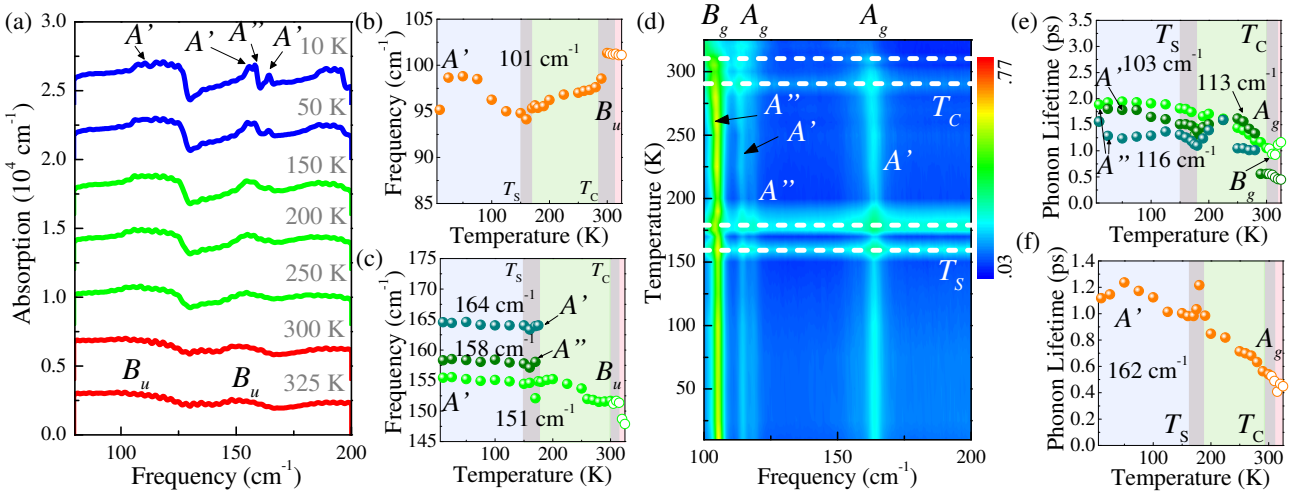

FIG. 5. Infrared (a-c) and Raman scattering (d-f) response of $CuInP_2S_6$ across the structural transition, T_S. Recall, high temperature spectra are shown in red and low temperature spectra are shown in blue. Panel (a) summarizes the infrared spectrum as a function of temperature, and panels (b, c) show peak position vs. temperature to reveal the infrared-active modes most influenced by T_S. The curves in panel (a) are off-set for clarity. Panel (c) summarizes the variable temperature Raman scattering spectrum in a contour plot, whereas panels (e, f) deepen our understanding of the structural transition by examining phonon lifetime trends (obtained line width effects as discussed in the text) as a function of temperature. There is a significant hysteresis effect depending upon direction of temperature sweep. This large hysteresis is seen very clearly in the Raman scattering response when rendered as a contour plot [Supplemental Information]. These measurements are from 10 K up to 325 K.

Clearly, subtle structural changes have important consequences for properties in this system.

C. Vibrational properties of $CuInP_2S_6$ across the structural phase transition

In addition to the well defined ferroelectric transition, $CuInP_2S_6$ displays a structural phase transition (T_S) near 150 K [Fig. 5]. By comparison, the structural transition is more subtle and much less studied than the ferroelectric transition. Signatures of T_S tend to be most pronounced in infrared- and Raman-active features below 200 cm^{-1}. These modes are mostly due to out-of-plane motions of indium and copper [Table S1 and S2].

We begin by examining the infrared response. Above T_C, we find two B_u symmetry phonons centered around 101 and 151 cm^{-1} [red curve, Fig. 5(a)]. We can track how these modes evolve across the 150 K structural transition using frequency vs. temperature plots [Fig. 5(b,c)]. The lower frequency B_u mode at 101 cm^{-1} shows a sharp jump across the ferroelectric transition, below which it becomes an A' symmetry mode. This feature red shifts until approximately 150 K, below which it begins blue shifting again. This strong inflection point in the frequency vs. temperature trend is consistent with a local structure distortion. The higher frequency B_u symmetry mode at 151 cm^{-1} is different. There is a systematic blue shift in the high temperature phase, an inflection point at T_C (below which the symmetry is A'), and continued hardening toward the structural phase transition. Below 150 K, this peak splits into a doublet - with features centered at 155 cm^{-1} (A') and 158 cm^{-1} (A'') - and a new peak at 164 cm^{-1} (A'). The latter is a weak signature of symmetry breaking. Below T_S, both branches of the doublet as well as the new feature show a slight, yet systematic blue shift toward base temperature.

Interestingly, Raman scattering spectroscopy reveals that the structural phase transition in $CuInP_2S_6$ may take place in two distinct steps. This is particularly noticeable in the contour plot [Fig. 5(d)]. Significant broadening of all three phonons is observed around 175 and 150 K - in addition to underlying scattering intensity consistent with order-disorder processes [41]. Similar underlying scattering is observed in multiferroic $RbFe(SO_4)_2$ [67]. We also analyzed the phonons of interest - this time by examining phonon lifetime vs. temperature trends. This quantity is calculated from the phonon linewidth and is an expression of Heisenberg uncertainty principle [68]. The lifetime of the B_g symmetry mode centered at 103 cm^{-1} decreases toward T_C (below which, the symmetry changes to A''), where there is a sharp upturn in phonon lifetime that continues until approximately 175 K where there is a small cusp, below which the phonon lifetime continues to rise into the low temperature phase. The ferroelectric A_g mode at 113 cm^{-1} [Fig. 5(d, f)] shows two-step broadening around T_C and splits into two features (A', A'') below 300 K. The phonon lifetime of the A' branch rises to a maximum near 200 K, shows cusps at both 175 and 150 K, and continues to rise toward base temperature. The A'' symmetry counterpart follows a similar trend, but is more pronounced. The

cusps at 175 and 150 K suggest that the structural phase transition has two steps. This is in line with prior dielectric studies that confirm a double step around the structural transition due to a freezing of the Cu^+ ions [36]. The Raman-active A_g symmetry mode near 162 cm^{-1} is also coupled to the structural distortion. The phonon lifetime of this feature rises systematically toward T_S and displays a pronounced cusp in the 175 to 150 K region before rising again.

Taken together, we see that while many infrared- and Raman-active features are responsible for driving the ferroelectric transition, the structural transition in $CuInP_2S_6$ is discernible only through subtle peak splitting and shifting. Moreover, evidence for the structural distortion appears primarily in the low frequency modes below 200 cm^{-1}, suggesting that T_S is connected with layer shifting or slight reorganization of the Cu^+ and In^{3+} centers (which may also impact the polarization). This distortion is consistent with the low frequency dielectric constant of $CuInP_2S_6$ which shows a broad transition region near 155 K along with evidence for a possible two-step structural transition embedded in the overall shape of the response at certain frequencies [36].

Intriguingly, members of the MPS_3 (M = Mn, Fe, Ni) family also display temperature driven structural distortions although they seem to be connected with magnetic ordering. For example, $MnPS_3$ hosts spin-phonon coupling across the antiferromagnetic ordering transition [69], and $NiPS_3$ shows evidence of two-magnon modes and the emergence of an exciton below 200 K [70]. The development of magnon modes is also see in Raman studies of $FePS_3$ below T_N = 118 K [10]. Aside from the emergence of these low frequency magnon modes, the MPS_3 systems remain largely unaffected by temperature alone, whereas $CuInP_2S_6$ is much more temperature sensitive. Much like members of the MPS_3 family, subtle structural distortions are evidenced in the features below 200 cm^{-1}.

D. Tendency toward chemical phase separation in $CuInP_2S_6$-like materials

$CuInP_2S_6$ is just one stable phase amongst many available within the rich temperature-composition phase diagram of $CuInS_2$ materials. The majority of other chemically-related compounds have only slightly different compositions and follow the general formula $Cu_{1-x}In_{1+x/3}P_2S_6$ [71]. This exceptional complexity makes growth of single crystals and quantum dots with the correct nominal composition quite challenging [71, 72]. At the same time, it is important to avoid phase segregation. Despite a number of prior reports, there is no consensus on the visual appearance of a high quality single crystal or the character of a Raman scattering spectrum at room temperature. This is because color changes with thickness, Cu concentration, and defect concentration, and a traditional Raman response averages over the presence of any chemical phase separation. Two principle varieties of Raman spectra have been reported for nominally stoichiometric crystals. One kind has well separated vibrational features whereas the other type has a more complicated pattern with clustered peaks [29, 33, 41, 64, 73–76]. As part of this work, we explored the origin of these differences in order to reveal the intrinsic properties of $CuInP_2S_6$. As described below, we uncover both phase pure $CuInP_2S_6$ as well as crystals with a segregated impurity phase. The impurity phase material is $In_{4/3}P_2S_6$ [71].

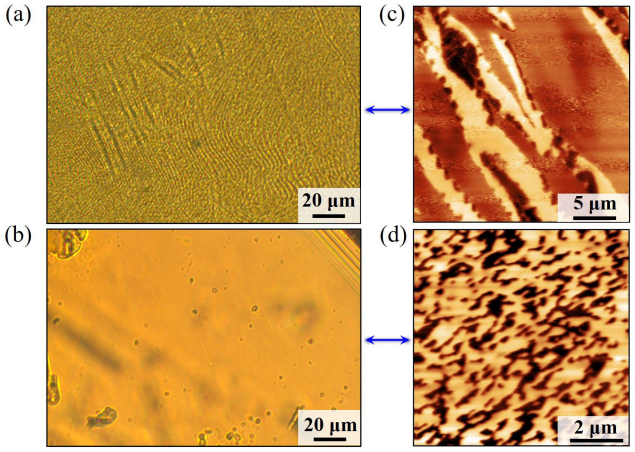

FIG. 6. (a, b) Comparison of optical microscope images taken in transmission for mixed-phase and pure $CuInP_2S_6$. (c, d) Vertical piezo-force microscopy images for mixed phase and pure $CuInP_2S_6$.

Chemical vapor transport growth of $CuInP_2S_6$ single crystals results in thin, orange, transparent flakes. We find, however, that two types of flakes with distinct thicknesses, colors, and sizes coexist - even in the same batch (Fig. S1, Supporting Information). The type-I flake has a large lateral dimension (3-10 mm) and reduced thickness (10-30 µm). It thus displays a lighter color than the second type with a lateral dimension of 0.5-1.0 mm and a thickness of 70-150 µm. Figure 6(a,b) displays transmission optical microscope images of both specimens with 50× magnification. The type-II $CuInP_2S_6$ crystal has a homogeneous orange color without additional patterns inside the crystal whereas the type-I crystal has wavy stripes with dark/bright contrast.

To understand the difference between the two types of $CuInP_2S_6$ and what causes the wavy stripes observed in the type-I sample, we took vertical piezo-force microscopy images on freshly exfoliated surfaces at room temperature. When the temperature is below T_C, $CuInP_2S_6$ exhibits a spontaneous polarization perpendicular to the layered planes which originates from the off-center ordering of the Cu sublattice and the slight displacement of In cations from the sulfur octahedral center [Fig. 1]. This atomic arrangement gives rise to two possible ferroelectric variants with opposite polarization di-

rections perpendicular to the layered planes. As a result, we expect a bipolar response.

Figure 6(c,d) displays the vertical piezo-force microscopy images for the two specimens. For the type-I sample, we find two kinds of alternating wavy stripes and three kinds of coexisting domains. One type of stripe contains two domains showing dark and bright colors, whereas the adjacent stripes display a single color. The size of these stripes is comparable to those observed in the optical microscope image [Fig. 6(b)]. For the type-II sample, we find irregular island domains with two different colors. The two kinds of domains in the type-II sample should correspond to the two possible ferroelectric variants. As for the three kinds of domains in the type-I sample, since there exists only two possible ferroelectric variants [Fig. 1], we can conclude that the type-I $CuInP_2S_6$ contains a significant impurity phase in addition to the two separate phases that form into alternating wavy stripes. This impurity phase is directly confirmed to be Cu-deficient $In_{4/3}P_2S_6$ via transmission electron microscopy [77].

Figure 7 shows the phase-separated image and selected area electron diffraction (SAED) patterns of $CuInP_2S_6$ along [100] and [001], respectively. $In_{4/3}P_2S_6$ and $CuInP_2S_6$ coexist within the crystal by aligning along the b-axes to maintain the layered structural framework. Intriguingly, we find that phase-separated patterns vary and include alternating wavy stripes, straight stripes, rectangular blocks, among others. Vertical piezo-force microscopy images showing these patterns are available in Fig. S2, Supporting Information. Clearly phase separation can be quite robust. The domain size depends upon the cooling rate [71]. These two polar domains split into four under strain [27, 28].

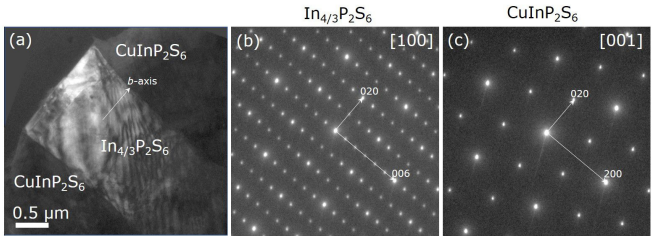

FIG. 7. (a) In-plane TEM images of $CuInP_2S_6$ crystal, revealing local phase separation. The bright and dark areas with sharp phase boundaries represent $In_{4/3}P_2S_6$ and $CuInP_2S_6$, respectively. Selected area electron diffraction patterns taken on regions of (b) $In_{4/3}P_2S_6$ and (c) $CuInP_2S_6$ shown in (a).

Figure 8(a) summarizes the Raman response of $CuInP_2S_6$, a mixed phase crystal, and $In_{4/3}P_2S_6$. Clearly, the Raman scattering spectrum of the mixed phase sample is a superposition of the other two. Unfortunately, the spectrum of the mixed phase material appears very commonly in the literature [64, 75, 76] - usually incorrectly identified as the pure phase $CuInP_2S_6$. As demonstrated above, a detailed analysis of composition, electron diffraction, and piezoforce microscopy was needed to unravel the situation, and now that we have linked these properties with the character of the Raman spectrum, phase identification will be much easier. Assuming that the spectrum of the mixed phase sample is a straightforward superposition of $CuInP_2S_6$ and $In_{4/3}P_2S_6$, we can estimate an impurity phase concentration by a simple ratio analysis [78]. We find that the crystal with chemical phase separation may contain as much as 80% $In_{4/3}P_2S_6$. This analysis obviously assumes that the response of the mixed phase system is a linear combination of the characteristics of the two end members. Characteristic signatures of $In_{4/3}P_2S_6$ inclusions include: (i) a strong doublet centered between 125 and 145 cm^{-1} as well as (ii) a multi-peak cluster between 230 and 300 cm^{-1}. The spectrum of pure phase $CuInP_2S_6$ is simpler with well-separated peaks. The mode positions are also in good agreement with our dynamics calculations, which can be found in the Supporting Information [63]. All of the work presented in this paper was performed on high quality, pure phase $CuInP_2S_6$ single crystals. As discussed above, piezoforce microscopy reveals that these crystals have two polar phases (up and down).

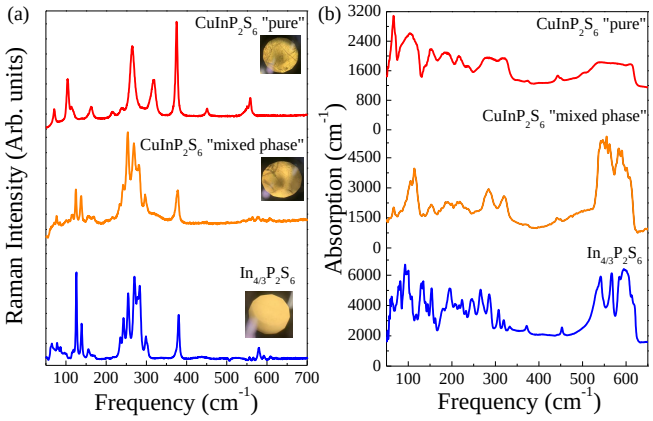

FIG. 8. Comparison of the (a) Raman scattering and (b) infrared absorption of the pure and mixed phase $CuInP_2S_6$ as well as the impurity phase $In_{4/3}P_2S_6$. All spectra are taken at 300 K.

Figure 8(b) shows the infrared absorption of phase pure $CuInP_2S_6$, a mixed phase sample, and $In_{4/3}P_2S_6$. Overall, the spectra are similar to what is found in the MPS_3 (M = Mn, Fe, Ni) series [79] except for the additional mode splitting due to the chemical and structural complexity on the metal site. Our mode assignments are summarized in Tables S1 and S2 in the Supporting Information [63].

SUMMARY AND OUTLOOK

In order to explore the properties of complex chalcogenides, we measured the infrared absorption and Raman scattering response of $CuInP_2S_6$ across the ferroelectric

and structural phase transitions and compared our findings with a symmetry analysis and complementary lattice dynamics calculations. Several different infrared- and Raman-active modes drive the ferroelectric transition whereas the structural transition is characterized by much more subtle peak splitting and shifting. Both transitions have large hysteresis regions - probably on account of the bimetallic nature of this system. The structural transition is different in that it has significant underlying scattering intensity as well - surprisingly similar to what is found across order-disorder transitions in certain multiferroics. We also investigated the tendency toward chemical phase separation in these materials and, using a combination of optical microscopy, piezoforce microscopy, transmission electron microscopy, and vibrational spectroscopies, we unravel the signature of the highest quality crystals. The latter has two (rather than three) unique polar phases corresponding to "up" and "down" polarizations, respectively. The impurity phase in the mixed sample is determined to be $In_{4/3}P_2S_6$. This work places the vibrational properties of ferroelectric $CuInP_2S_6$ on a firm foundation and supports future work to reveal the symmetry and dynamics of few- and single-layer systems.

ACKNOWLEDGEMENTS

Research at the University of Tennessee is supported by the U.S. Department of Energy, Office of Basic Energy Sciences, Materials Science Division under award DE-FG02-01ER45885. Work at Rutgers University is funded by the National Science Foundation DMREF program (DMR-1629059). Work at Pohang University of Science and Technology was supported by the National Research Foundation of Korea (NRF) funded by the Ministry of Science and ICT (No. 2016K1A4A4A01922028). S.S., K.M.R., and D.V. acknowledge the support from ONR grants N00014-16-1-2951 and N00014-19-1-2073.

[1] Burch, K. S., Mandrus, D., & Park, J.-G. Magnetism in two-dimensional van der Waals materials. *Nature* **563**, 47–52 (2018).

[2] McGuire, M. A. Cleavable magnetic materials from van der Waals layered transition metal halides and chalcogenides. *Journal of Applied Physics* **128**, 110901 (2020).

[3] Wang, M. C., Huang, C. C., Cheung, C. H., Chen, C. Y., Tan, S. G., Huang, T. W., Zhao, Y., Zhao, Y., Wu, G., Feng, Y. P., Wu, H. C., & Chang, C. R. Prospects and Opportunities of 2D van der Waals Magnetic Systems. *Annalen der Physik* **532**, 1–19 (2020).

[4] Haines, C. R., Coak, M. J., Wildes, A. R., Lampronti, G. I., Liu, C., Nahai-Williamson, P., Hamidov, H., Daisenberger, D., & Saxena, S. S. Pressure-induced electronic and structural phase evolution in the van der Waals compound $FePS_3$. *Phys. Rev. Lett.* **121**, 266801 (2018).

[5] Wang, Y., Ying, J., Zhou, Z., Sun, J., Wen, T., Zhou, Y., Li, N., Zhang, Q., Han, F., Xiao, Y., Chow, P., Yang, W., Struzhkin, V. V., Zhao, Y., & Mao, H. K. Emergent superconductivity in an iron-based honeycomb lattice initiated by pressure-driven spin-crossover. *Nature Communications* **9**, 1914 (2018).

[6] Harms, N., Kim, H.-S., Clune, A. J., Smith, K., O'Neal, K. R., Haglund, A., Mandrus, D. G., Liu, Z., Haule, K., Vanderbilt, D., & Musfeldt, J. L. Piezochromism in the magnetic chalcogenide $MnPS_3$. *Nat. Quantum Mater.* **5**, 56 (2020).

[7] Coak, M. J., Jarvis, D. M., Hamidov, H., Wildes, A. R., Paddison, J. A. M., Liu, C., Haines, C. R. S., Dang, N. T., Kichanov, S. E., Savenko, B. N., Lee, S., Kratochvílová, M., Klotz, S., & Hansen, T. C. Emergent Magnetic Phases in Pressure-Tuned van der Waals Antiferromagnet $FePS_3$. *Physical Review X* **11**, 11024 (2021).

[8] Wildes, A. R., Lançon, D., Chan, M. K., Weickert, F., Harrison, N., Simonet, V., Zhitomirsky, M. E., Gvozdikova, M. V., Ziman, T., & Rønnow, H. M. High field magnetization of $FePS_3$. *Physical Review B* **101**, 24415 (2020).

[9] Wang, X., Cao, J., Lu, Z., Cohen, A., Kitadai, H., Li, T., Tan, Q., Wilson, M., Lui, C. H., Smirnov, D., Sharifzadeh, S., & Ling, X. Spin-induced linear polarization of photoluminescence in antiferromagnetic van der Waals crystals. *Nature Materials* (2021).

[10] McCreary, A., Simpson, J. R., Mai, T. T., McMichael, R. D., Douglas, J. E., Butch, N., Dennis, C., Valdés Aguilar, R., & Hight Walker, A. R. Quasi-two-dimensional magnon identification in antiferromagnetic $FePS_3$ via magneto-raman spectroscopy. *Phys. Rev. B* **101**, 064416 (2020).

[11] Alliati, I. M., Evans, R. F. L., Novoselov, K. S., & Santos, E. J. G. Ultrafast current and field driven domain-wall dynamics in van der Waals antiferromagnet $MnPS_3$. *arXiv Cond-Mat.mes-hall* 1–29 (2020).

[12] Wang, F., Shifa, T. A., Yu, P., He, P., Liu, Y., Wang, F., Wang, Z., Zhan, X., Lou, X., Xia, F., & He, J. New Frontiers on van der Waals layered metal phosphorous trichalcogenides. *Adv. Funct. Mater.* **28**, 1802151 (2018).

[13] Kargar, F., Coleman, E. A., Ghosh, S., Lee, J., Gomez, M. J., Liu, Y., Magana, A. S., Barani, Z., Mohammadzadeh, A., Debnath, B., Wilson, R. B., Lake, R. K., & Balandin, A. A. Phonon and thermal properties of quasi-two-dimensional $FePS_3$ and $MnPS_3$ antiferromagnetic semiconductors. *ACS Nano* **14**, 2424–2435 (2020).

[14] Kaul, A. B. Two-dimensional layered materials: Structure, properties, and prospects for device applications. *J. Mater. Res.* **29**, 348–361 (2014).

[15] Huang, B., Clark, G., Navarro-Moratalla, E., Klein, D. R., Cheng, R., Seyler, K. L., Zhong, D., Schmidgall, E., McGuire, M. A., Cobden, D. H., Yao, W., Xiao, D., Jarillo-Herrero, P., & Xu, X. Layer-dependent ferromagnetism in a van der Waals crystal down to the monolayer limit. *Nature* **546**, 270–273 (2017).

[16] Kim, K., Lim, S. Y., Lee, J. U., Lee, S., Kim, T. Y., Park, K., Jeon, G. S., Park, C. H., Park, J. G., & Cheong, H. Suppression of magnetic ordering in XXZ-type antiferromagnetic monolayer $NiPS_3$. *Nat. Commun.* **10**, 345 (2019).

[17] Long, G., Zhang, T., Cai, X., Hu, J., Cho, C. W., Xu, S., Shen, J., Wu, Z., Han, T., Lin, J., Wang, J., Cai, Y., Lortz, R., Mao, Z., & Wang, N. Isolation and characterization of few-layer manganese thiophosphite. *ACS Nano* **11**, 11330–11336 (2017).

[18] Sun, Y.-J., Tan, Q.-H., Liu, X.-L., Gao, Y.-F., & Zhang, J. Probing the magnetic ordering of antiferromagnetic $MnPS_3$ by Raman spectroscopy. *J. Phys. Chem. Lett.* **10**, 3087–3093 (2019).

[19] Zhang, X., Qiao, X.-F., Shi, W., Wu, J.-B., Jiang, D.-S., & Tan, P.-H. Phonon and Raman scattering of two-dimensional transition metal dichalcogenides from monolayer to bulk material. *Chem. Soc. Rev.* **44**, 2757–2785 (2015).

[20] Kuo, C. T., Neumann, M., Balamurugan, K., Park, H. J., Kang, S., Shiu, H. W., Kang, J. H., Hong, B. H., Han, M., Noh, T. W., & Park, J. G. Exfoliation and Raman Spectroscopic Fingerprint of Few-Layer $NiPS_3$ Van der Waals Crystals. *Sci. Rep.* **6**, 20904 (2016).

[21] Lee, J. Y., Shin, J. H., Lee, G. H., & Lee, C. H. Two-dimensional semiconductor optoelectronics based on van der Waals heterostructures. *Nanomaterials* **6**, 193 (2016).

[22] Zhong, L., Chen, X., & Qi, J. Controlling the spin and valley degeneracy splitting in monolayer $MnPSe_3$ by atom doping. *Phys. Chem. Chem. Phys.* **19**, 15388–15393 (2017).

[23] Chu, H., Roh, C. J., Island, J. O., Li, C., Lee, S., Chen, J., Park, J. G., Young, A. F., Lee, J. S., & Hsieh, D. Linear Magnetoelectric Phase in Ultrathin $MnPS_3$ Probed by Optical Second Harmonic Generation. *Phys. Rev. Lett.* **124**, 027601 (2020).

[24] Kurumaji, T., Ishiwata, S., & Tokura, Y. Doping-tunable ferrimagnetic phase with large linear magnetoelectric effect in a polar magnet $Fe_2Mo_3O_8$. *Physical Review X* **5**, 031034 (2015).

[25] Xu, K., Lu, X. Z., & Xiang, H. Designing new ferroelectrics with a general strategy. *npj Quantum Materials* **2**, 1906 (2017).

[26] Osada, M. & Sasaki, T. The rise of 2D dielectrics/ ferroelectrics. *APL Materials* **7**, 120902 (2019).

[27] Brehm, J. A., Neumayer, S. M., Tao, L., Hara, A. O., Chyasnavichus, M., Susner, M. A., McGuire, M. A., Kalinin, S. V., Jesse, S., Ganesh, P., Pantelides, S. T., Maksymovych, P., & Balke, N. Tunable quadruple-well ferroelectic van der Waals crystals. *Nature Materials* **19**, 43–48 (2020).

[28] Neumayer, S. M., Brehm, J. A., Tao, L., O'Hara, A., Ganesh, P., Jesse, S., Susner, M. A., McGuire, M. A., Pantelides, S. T., Maksymovych, P., & Balke, N. Local strain and polarization mapping in ferrielectric materials. *ACS Applied Materials & Interfaces* **12**, 38546–38553 (2020).

[29] Grzechnik, A., Cajipe, V. B., Payen, C., & McMillan, P. F. Pressure-induced phase transition in ferrielectric $CuInP_2S_6$. *Solid State Commun.* **108**, 43–47 (1998).

[30] Simon, A., Ravez, J., Maisonneuve, V., Payen, C., & Cajipe, V. B. Paraelectric-ferroelectric transition in the lamellar thiophosphate $CuInP_2S_6$. *Chem. Mater.* **6**, 1575–1580 (1994).

[31] Maisonneuve, V., Evain, M., Payen, C., Cajipe, V. B., & Molinié, P. Room-temperature crystal structure of the layered phase $CuInP_2S_6$. *J. Alloys Compd.* **218**, 157–164 (1995).

[32] Fagot-Revurat, Y., Bourdon, X., Bertran, F., Cajipe, V. B., & Malterre, D. Interplay between electronic and crystallographic instabilities in the low-dimensional ferroelectric CuInP2se6. *Journal of Physics: Condensed Matter* **15**, 595–602 (2003).

[33] Liu, F., You, L., Seyler, K. L., Li, X., Yu, P., Lin, J., Wang, X., Zhou, J., Wang, H., He, H., Pantelides, S. T., Zhou, W., Sharma, P., Xu, X., Ajayan, P. M., Wang, J., & Liu, Z. Room-temperature ferroelectricity in $CuInP_2S_6$ ultrathin flakes. *Nat. Commun.* **7**, 1–6 (2016).

[34] Belianinov, A., He, Q., Dziaugys, A., Maksymovych, P., Eliseev, E., Borisevich, A., Morozovska, A., Banys, J., Vysochanskii, Y., & Kalinin, S. $CuInP_2S_6$ room temperature layered ferroelectric. *Nano Lett.* **15**, 3808–3814 (2015).

[35] Dziaugys, A., Kelley, K., Brehm, J. A., Tao, L., Puretzky, A., Feng, T., O'Hara, A., Neumayer, S., Chyasnavichyus, M., Eliseev, E. A., Banys, J., Vysochanskii, Y., Ye, F., Chakoumakos, B. C., Susner, M. A., McGuire, M. A., Kalinin, S. V., Ganesh, P., Balke, N., Pantelides, S. T., Morozovska, A. N., & Maksymovych, P. Piezoelectric domain walls in van der waals antiferroelectric $CuInP_2Se_6$. *Nature Communications* **11**, 3623 (2020).

[36] Dziaugys, A., Banys, J., MacUtkevic, J., Sobiestianskas, R., & Vysochanskii, Y. Dipolar glass phase in ferrielectrics: $CuInP_2S_6$ and $Ag_0.1Cu_0.9InP_2S_6$ crystals. *Phys. Status Solidi Appl. Mater. Sci.* **207**, 1960–1967 (2010).

[37] Maisonneuve, V., Cajipe, V. B., Simon, A., Von Der Muhll, R., & Ravez, J. Ferrielectric ordering in lamellar $CuInP_2S_6$. *Phys. Rev. B* **56**, 10860–10868 (1997).

[38] Bercha, D. M., Bercha, S. A., Glukhov, K. E., & Sznajder, M. Vibronic interaction in crystals with the Jahn-Teller centers in the elementary energy bands concept. *Condens. Matter Phys.* **18**, 1–17 (2015).

[39] Neumayer, S. M., Tao, L., O'Hara, A., Brehm, J., Si, M., Liao, P.-Y., Feng, T., Kalinin, S. V., Ye, P. D., Pantelides, S. T., Maksymovych, P., & Balke, N. Alignment of polarization against an electric field in van der waals ferroelectrics. *Phys. Rev. Applied* **13**, 064063 (2020).

[40] S, W. F. C., Zhang, D., Luo, Z.-d., Yao, Y., Schoenherr, P., Sha, C., Pan, Y., Sharma, P., Alexe, M., & Seidel, J. Anisotropic ion migration and electronic conduction in van der Waals ferroelectric $CuInP_2S_6$. *Nano Letters* **21**, 995–1002 (2021).

[41] Vysochanskii, Y. M., Stephanovich, V., Molnar, A., Cajipe, V., & Bourdon, X. Raman spectroscopy study of the ferrielectric-paraelectric transition in layered. *Phys. Rev. B - Condens. Matter Mater. Phys.* **58**, 9119–9124 (1998).

[42] Si, M., Saha, A. K., Liao, P. Y., Gao, S., Neumayer, S. M., Jian, J., Qin, J., Balke Wisinger, N., Wang, H., Maksymovych, P., Wu, W., Gupta, S. K., & Ye, P. D. Room-temperature electrocaloric effect in layered ferroelectric $CuInP_2S_6$ for solid-state refrigeration. *ACS Nano* **13**, 8760–8765 (2019).

[43] You, L., Zhang, Y., Zhou, S., Chaturvedi, A., Morris, S. A., Liu, F., Chang, L., Ichinose, D., Funakubo, H., Hu, W., Wu, T., Liu, Z., Dong, S., & Wang, J. Origin of giant negative piezoelectricity in a layered van der waals ferroelectric. *Science Advances* **5**, eaav3780 (2019).

[44] Chyasnavichyus, M., Susner, M. A., Ievlev, A. V., Eliseev, E. A., Morozovska, A. N., McGuire, M. A.,

Maksymovych, P., Chyasnavichyus, M., Susner, M. A., Ievlev, A. V., Eliseev, E. A., Kalinin, S. V., Balke, N., Morozovska, A. N., & McGuire, M. A. Size-effect in layered ferrielectric $CuInP_2S_6$. *Applied Physics Letters* **109**, 172901 (2016).

[45] Chen, L., Li, Y., Li, C., Wang, H., Han, Z., Ma, H., Yuan, G., Lin, L., & Yan, Z. Thickness dependence of domain size in 2D ferroelectric $CuInP_2S_6$ nanoflakes. *AIP Advances* **9**, 115211 (2019).

[46] Zhu, Z., Chen, X., Li, W., & Qi, J. Electric field control of the semiconductor- metal transition in two dimensional $CuInP_2S_6$ / germanene van der Waals heterostructure. *Applied Physics Letters* **114**, 223102 (2019).

[47] Wang, X., Yu, P., Lei, Z., Zhu, C., Cao, X., Liu, F., You, L., Zeng, Q., Deng, Y., Zhu, C., Zhou, J., Fu, Q., Wang, J., Huang, Y., & Liu, Z. Van der Waals negative capacitance transistors. *Nature Communications* **10**, 3037 (2019).

[48] Kresse, G. & Furthmüller, J. Efficient iterative schemes for ab initio total-energy calculations using a plane-wave basis set. *Phys. Rev. B* **54**, 11169–11186 (1996).

[49] Kresse, G. & Furthmüller, J. Efficiency of ab-initio total energy calculations for metals and semiconductors using a plane-wave basis set. *Computational Materials Science* **6**, 15 – 50 (1996).

[50] Kresse, G. & Joubert, D. From ultrasoft pseudopotentials to the projector augmented-wave method. *Phys. Rev. B* **59**, 1758–1775 (1999).

[51] Perdew, J. P., Burke, K., & Ernzerhof, M. Generalized gradient approximation made simple. *Phys. Rev. Lett.* **77**, 3865–3868 (1996).

[52] Grimme, S., Antony, J., Ehrlich, S., & Krieg, H. A consistent and accurate ab initio parametrization of density functional dispersion correction (dft-d) for the 94 elements h-pu. *The Journal of Chemical Physics* **132**, 154104 (2010).

[53] Tawfik, S. A., Reimers, J. R., Stampfl, C., & Ford, M. J. van der waals forces control the internal chemical structure of monolayers within the lamellar materials $CuInP_2S_6$ and $CuBiP_2Se_6$. *The Journal of Physical Chemistry C* **122**, 22675–22687 (2018).

[54] Reimers, J. R., Tawfik, S. A., & Ford, M. J. van der waals forces control ferroelectric-antiferroelectric ordering in $CuInP_2S_6$ and $CuBiP_2Se_6$ laminar materials. *Chem. Sci.* **9**, 7620–7627 (2018).

[55] Monkhorst, H. J. & Pack, J. D. Special points for brillouin-zone integrations. *Phys. Rev. B* **13**, 5188–5192 (1976).

[56] Togo, A. & Tanaka, I. First principles phonon calculations in materials science. *Scr. Mater.* **108**, 1–5 (2015).

[57] Kroumova, E., Aroyo, M., Perez-Mato, J., Kirov, A., Capillas, C., Ivantchev, S., & Wondratschek, H. Bilbao crystallographic server : Useful databases and tools for phase-transition studies. *Phase Transitions* **76**, 155–170 (2003).

[58] Skelton, J. M., Burton, L. A., Jackson, A. J., Oba, F., Parker, S. C., & Walsh, A. Lattice dynamics of the tin sulphides SnS_2, SnS and Sn_2S_3: vibrational spectra and thermal transport. *Phys. Chem. Chem. Phys.* **19**, 12452–12465 (2017).

[59] Maisonneuve, V., Cajipe, V. B., & Payen, C. Low-temperature neutron powder diffraction study of copper chromium thiophosphate ($CuCrP_2S_6$): observation of an ordered, antipolar copper sublattice. *Chemistry of Materials* **5**, 758–760 (1993).

[60] Babuka, T., Glukhov, K., Vysochanskii, Y., & Makowska-Janusik, M. Layered ferrielectric crystals $CuInP_2S(Se)_6$: a study from the first principles. *Phase Transitions* **92**, 440–450 (2019).

[61] King-Smith, R. D. & Vanderbilt, D. Theory of polarization of crystalline solids. *Phys. Rev. B* **47**, 1651–1654 (1993).

[62] Resta, R. Macroscopic polarization in crystalline dielectrics: the geometric phase approach. *Rev. Mod. Phys.* **66**, 899–915 (1994).

[63] See Supporting Information at [XXX] for a comparison of experimental and theoretical phonon positions along with their corresponding displacement patterns, as well as piezoforce microscope images of phase separated $CuInP_2S_6$.

[64] Si, M., Liao, P. Y., Qiu, G., Duan, Y., & Ye, P. D. Ferroelectric field-effect transistors based on MoS_2 and $CuInP_2S_6$ two-dimensional van der Waals heterostructure. *ACS Nano* **12**, 6700–6705 (2018).

[65] Ressouche, E., Loire, M., Simonet, V., Ballou, R., Stunault, A., & Wildes, A. Magnetoelectric $MnPS_3$ as a candidate for ferrotoroidicity. *Phys. Rev. B* **82**, 100408(R) (2010).

[66] Neal, S. N., O'Neal, K. R., Haglund, A. V., Mandrus, D. G., Bechtel, H. A., Carr, G. L., Haule, K., Vanderbilt, D., Kim, H. S., & Musfeldt, J. L. Exploring few and single layer $CrPS_4$ with near-field infrared spectroscopy. *2D Materials* **8**, 035020 (2021).

[67] Yang, J., Neal, S. N., Tyson, T., & Musfeldt, J. L. *In preparation* (2021).

[68] Sun, Q. C., Mazumdar, D., Yadgarov, L., Rosentsveig, R., Tenne, R., & Musfeldt, J. L. Spectroscopic determination of phonon lifetimes in rhenium-doped MoS_2 nanoparticles. *Nano Lett.* **13**, 2803–2808 (2013).

[69] Vaclavkova, D., Delhomme, A., Faugeras, C., Potemski, M., Bogucki, A., Suffczyński, J., Kossacki, P., Wildes, A. R., Grémaud, B., & Saúl, A. Magnetoelastic interaction in the two-dimensional magnetic material MnPS3 studied by first principles calculations and raman experiments. *2D Materials* **7**, 035030 (2020).

[70] Kang, S., Kim, K., Kim, B. H., Kim, J., Sim, K. I., Lee, J. U., Lee, S., Park, K., Yun, S., Kim, T., Nag, A., Walters, A., Garcia-Fernandez, M., Li, J., Chapon, L., Zhou, K. J., Son, Y. W., Kim, J. H., Cheong, H., & Park, J. G. Coherent many-body exciton in van der Waals antiferromagnet $NiPS_3$. *Nature* **583**, 785–789 (2020).

[71] Susner, M. A., Chyasnavichyus, M., McGuire, M. A., Ganesh, P., & Maksymovych, P. Metal Thio- and Selenophosphates as Multifunctional van der Waals Layered Materials. *Adv. Mater.* **29**, 1–39 (2017).

[72] Chen, Y., Li, S., Huang, L., & Pan, D. Green and facile synthesis of water-soluble Cu–In–S/ZnS core/shell quantum dots. *Inorganic Chemistry* **52**, 7819–7821 (2013).

[73] Bourdon, X. & Cajipe, V. B. Soft-Chemistry Forms of $Sn_2P_2S_6$ and $CuInP_2S_6$. *Journal of Solid State Chemistry* **141**, 290–293 (1998).

[74] Niu, L., Liu, F., Zeng, Q., Zhu, X., Wang, Y., Yu, P., Shi, J., Lin, J., Zhou, J., Fu, Q., Zhou, W., Yu, T., Liu, X., & Liu, Z. Controlled synthesis and room-temperature pyroelectricity of $CuInP_2S_6$ ultrathin flakes. *Nano Energy* **58**, 596–603 (2019).

[75] Susner, M. A., Chyasnavichyus, M., Puretzky, A. A., He, Q., Conner, B. S., Ren, Y., Cullen, D. A., Ganesh, P.,

Shin, D., Demir, H., McMurray, J. W., Borisevich, A. Y., Maksymovych, P., & McGuire, M. A. Cation-Eutectic transition via sublattice melting in $CuInP_2S_6/In_{4/3}P_2S_6$ van der Waals layered crystals. *ACS Nano* **11**, 7060–7073 (2017).

[76] Ievlev, A. V., Susner, M. A., McGuire, M. A., Maksymovych, P., & Kalinin, S. V. Quantitative analysis of the local phase transitions induced by laser heating. *ACS Nano* **9**, 12442–12450 (2015).

[77] Susner, M. A., Belianinov, A., Borisevich, A., He, Q., Chyasnavichyus, M., Demir, H., Sholl, D. S., Ganesh, P., Abernathy, D. L., McGuire, M. A., *et al.* High-T_c layered ferrielectric crystals by coherent spinodal decomposition. *ACS Nano* **9**, 12365–12373 (2015).

[78] Xu, X. S., Ihlefeld, J. F., Lee, J. H., Ezekoye, O. K., Vlahos, E., Ramesh, R., Gopalan, V., Pan, X. Q., Schlom, D. G., & Musfeldt, J. L. Tunable band gap in $Bi(Fe_{1-x}Mn_x)O_3$ films. *Applied Physics Letters* **96**, 192901 (2010).

[79] Neal, S., Kim, H.-S., O'Neal, K., Haglund, A., Smith, K., Mandrus, D., Bechtel, H., Carr, G. L., Haule, K., Vanderbilt, D., & Musfeldt, J. L. Symmetry crossover in layered MPS_3 complexes (M = Mn, Fe, Ni) via near-field infrared spectroscopy. *Phys. Rev. B* **102**, 085408 (2020).